

## Article

# The Resistance to Wear and Thermal Cracking of Laser Surface Engineered P20 Steel

Kangpei Zhao <sup>1</sup>, Guanghua Yan <sup>1</sup>, Jinhong Li <sup>2</sup>, Wenwu Guo <sup>3</sup>, Jianfeng Gu <sup>4</sup> and Chuanwei Li <sup>4,\*</sup> <sup>1</sup> School of Construction Machinery, Shandong Jiao Tong University, Jinan 250357, China<sup>2</sup> Academic Affairs Division, Qilu University of Technology, Jinan 250353, China<sup>3</sup> Tongyu Heavy Industry Co., Ltd., Dezhou 251200, China<sup>4</sup> Institute of Materials Modification and Modeling, School of Materials Science and Engineering, Shanghai Jiao Tong University, Shanghai 200240, China

\* Correspondence: li-chuanwei@sjtu.edu.cn

**Abstract:** This study reports the microstructure and surface properties of P20 steel processed by laser surface engineering (involving surface hardening and melting), which are carried out using a fiber laser with the maximum power of 2 kW. Ultrafine martensite laths with high boundary density are formed both in the laser surface hardened layer and in the melted layer. This dramatically improves the surface hardness of the P20 steel. However, the laser surface melted layer exhibits a relatively lower hardness than the laser surface hardened layer. It can be attributed to the remarkable autotempering effect and the vaporization of alloy elements in the melted layer. The wear resistance and thermal cracking resistance of the samples treated by laser surface engineering show a significant improvement compared with the as received material. The surface hardened layer exhibits superior wear and thermal cracking resistance due to its relatively high surface hardness and plastic deformation resistance, which can effectively suppress the formation of cracks during wear and thermal cracking tests.

**Keywords:** laser surface engineering; P20 steel; hardness; wear resistance; thermal cracking resistance



**Citation:** Zhao, K.; Yan, G.; Li, J.; Guo, W.; Gu, J.; Li, C. The Resistance to Wear and Thermal Cracking of Laser Surface Engineered P20 Steel. *Coatings* **2023**, *13*, 97. <https://doi.org/10.3390/coatings13010097>

Academic Editor: Ajay Vikram Singh

Received: 14 December 2022

Revised: 28 December 2022

Accepted: 3 January 2023

Published: 5 January 2023



**Copyright:** © 2023 by the authors. Licensee MDPI, Basel, Switzerland. This article is an open access article distributed under the terms and conditions of the Creative Commons Attribution (CC BY) license (<https://creativecommons.org/licenses/by/4.0/>).

## 1. Introduction

As a medium carbon low alloy tool steel, P20 is widely used in the fabrication of plastic injection molds [1]. It provides excellent polishing performance and toughness for these molds in its service temperature range of 200–250 °C. However, the hardness of this steel is not high enough in certain circumstances [2]. As a result, wear failure and thermal fatigue damage often occur during service process, thus shortening the service life of the molds. Therefore, excellent resistance to wear and thermal cracking is expected for the P20 plastic injection molds to prolong their service life. As well known, both wear and thermal cracking are closely associated with surface characteristics, such as surface microstructure, hardness profile, plastic deformation resistance, surface residual stress and topography [3–6]. Generally, smooth surfaces with residual compressive stress can effectively delay the occurrence of wear and the formation of thermal cracks [3,4]. In steels, martensite with high hardness and plastic deformation resistance is regarded as a desired microstructure to resist the formation of cracks caused by plastic deformation under the cyclic loading during wear and thermal process [5,6]. Hence, surface treatment is often performed on the steel components to obtain martensite for the enhanced wear and thermal cracking resistance.

As a surface modification method, laser surface engineering (LSE) is widely used in industrial manufacturing due to its high efficiency in improving surface properties, such as hardness, wear resistance and fatigue resistance [7,8]. Plenty of applications of LSE have been reported in the past decades. The purposes of these applications can be summarized into the following three aspects: improving wear resistance [9–11], improving corrosion

resistance [12–15] and improving fatigue resistance [16]. The process parameters of LSE, such as laser power and scanning speed, play a decisive role in determining the surface properties. Laser scanning speed directly determines the heat input of the surface material. Therefore, the surface layers processed by LSE with different scanning speed undergo different cycles of heating and cooling, which significantly influences the surface properties of the treated material. It is known that the scanning speed will influence the microstructure stability and hardness profile of the laser-modified layer [17–19]. Colaco et al. [17] indicated that a low scanning speed could reduce the content of austenite retained in the laser surface melted layer. Ameri et al. [18] demonstrated that a high heat input at a low scanning speed resulted in a high surface hardness. Apparently, LSE must be controlled and implemented at an appropriate scanning speed to provide the best microstructure and properties for surface material.

The purpose of the present work is to investigate the influence of LSE treatment with different scanning speeds on the microstructure and surface properties of P20 steel. LSE is performed at a laser power of 1300 W with different scanning speed to induce surface melting or hardening. The surface melted layer and hardened layer are compared with the as received (AR) material in respect of microstructure, hardness, wear and thermal cracking resistance. Then, the mechanism of surface properties improvement caused by LSE is clarified.

## 2. Materials and Methods

A commercial P20 steel pre-hardened to average hardness of  $350 \pm 15$  HV is received as the initial material. Its chemical composition shown in Table 1 is obtained using an optical emission spectrometer (Thermo Fisher Scientific ARL 4460, Waltham, MA, USA). Plate-like samples (11 mm × 45 mm × 80 mm) are machined from the AR material for LSE treatment. The surfaces of these samples are prepared by grinding and washing with acetone to ensure consistency in absorption of laser energy. A fiber laser with maximum power of 2 kW, wavelength of 1060 nm and flat top energy distribution of 10 mm × 1 mm is used to execute LSE treatment. Pure argon serves as the shielding gas to protect the sample surface from oxidation during laser process.

**Table 1.** Chemical composition (wt.%) of the P20 steel in different states.

| Steel State | C    | Si   | Mn   | Cr   | Mo   | V     | Al     | Fe   |
|-------------|------|------|------|------|------|-------|--------|------|
| AR          | 0.39 | 0.25 | 1.51 | 1.98 | 0.22 | 0.013 | 0.025  | Bal. |
| LSM-2 mm/s  | 0.39 | 0.03 | 0.76 | 1.66 | 0.22 | 0.006 | <0.005 | Bal. |
| LSH-4 mm/s  | 0.39 | 0.22 | 1.41 | 1.77 | 0.21 | 0.012 | 0.020  | Bal. |

The LSE are carried out at different laser powers (1100 W, 1300 W and 1500 W) with different scanning speeds (0.5–9 mm/s). Surface hardness and depth of the laser modified layers are summarized in Figure 1. It can be seen that 1300 W (65% of the maximum laser power) is an appropriate laser power for investigating the influences of laser surface melting (LSM) and laser surface hardening (LSH) due to the suitable surface hardness and depth of the modified layers formed at this power with scanning speed from 0.5 to 5 mm/s. Cross sectional observations of the samples laser surface treated at 1300 W are conducted on an optical microscopy (OM, ZEISS AXIO Observer A1m), and the results are shown in Figure 2. It can be seen that the depth of the laser-modified layer increases with decreasing scanning speed. Surface melted layers are observed in Figure 2a–c, indicating that low scanning speed ( $\leq 2$  mm/s) leads to the occurrence of surface melting. In Figure 2d–f, only the hardened layers are observed, indicating that surface melting is avoided with a high scanning speed ( $\geq 3$  mm/s). Therefore, LSE treatments at 1300 W with scanning speed lower than 2 mm/s and higher than 3 mm/s are named as LSM treatment and LSH treatment, respectively, in the present work. The microstructures and surface properties of the representative samples with scanning speed of 2 mm/s and 4 mm/s are characterized

in detail to analyze the effect of LSM and LSH treatment. After LSE treatment, the chemical composition of the surface layers of the LSM-2 mm/s and LSH-4 mm/s samples are measured using the optical emission spectrometer (Thermo Fisher Scientific ARL 4460) again, and the results are also listed in Table 1.

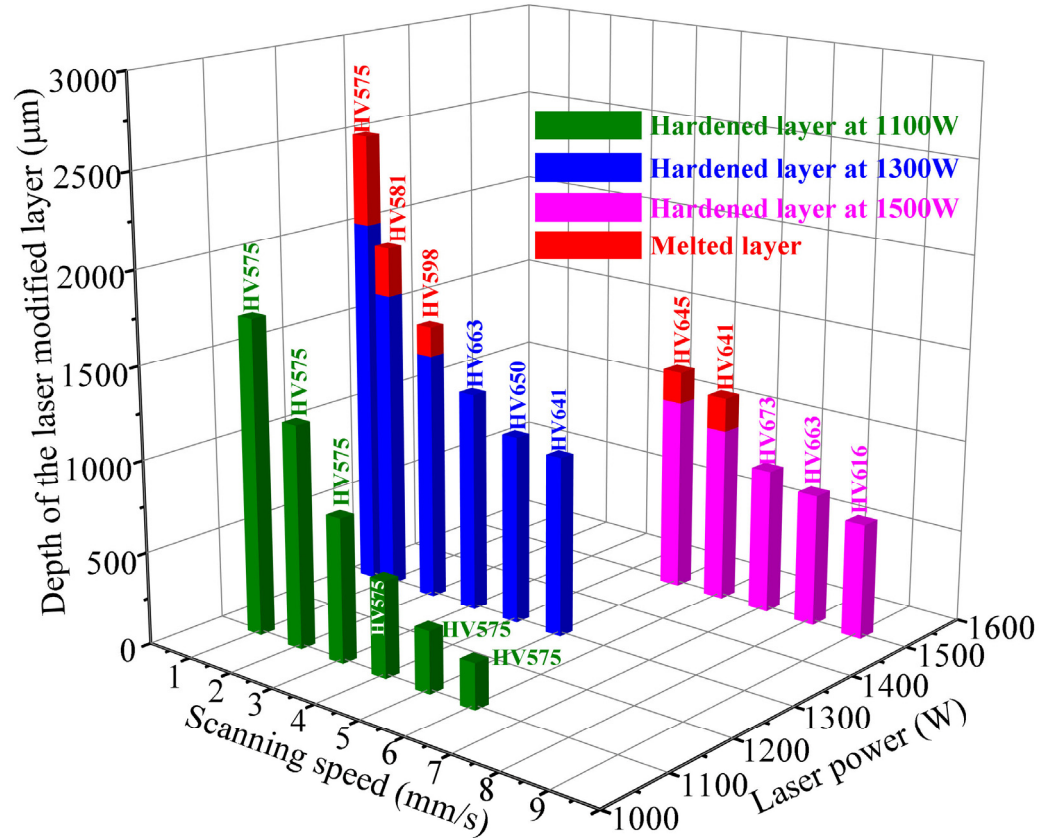


Figure 1. Surface hardness and depth of the laser modified layers obtained at different laser powers with different scanning speeds.

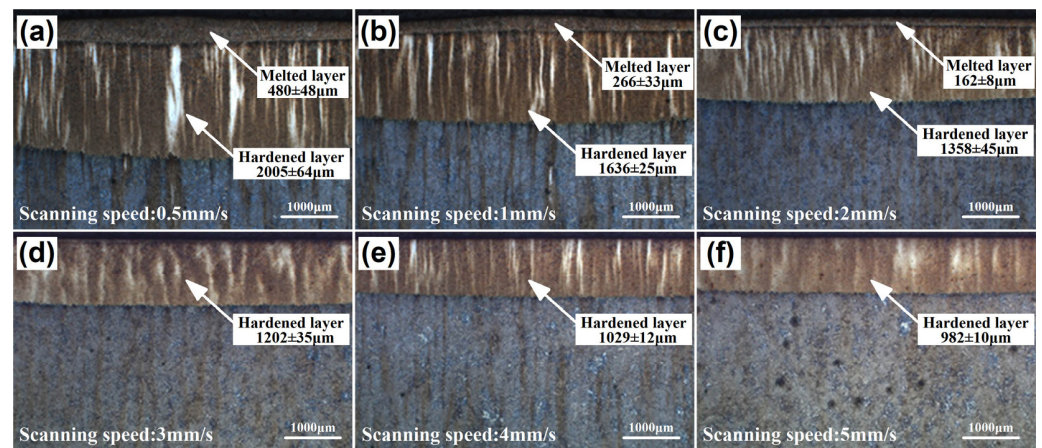


Figure 2. The macrostructures on the cross section of samples processed with 1300 W. (a) 0.5 mm/s, (b) 1 mm/s, (c) 2 mm/s, (d) 3 mm/s, (e) 4 mm/s, (f) 5 mm/s.

Cross-sectional microstructures of surface melted layer and hardened layer are examined using a scanning electron microscopy (SEM, TSCAN LYRA3) equipped with electron backscatter diffraction (EBSD) fast acquisition system (Oxford Instruments NordlysMax3). EBSD measurements are operated at an accelerating voltage of 20 kV, a working distance of 9 mm and a step size of 0.2  $\mu\text{m}$ . Afterwards, the commercial CHANNEL 5 software

provided by HKL Technology is used to process the EBSD data. The EBSD specimens are prepared using a nano chemical mechanical polisher (Buehler EcoMet 250, Lake Bluff, IL, USA). The preparation process is as follows: conventional mechanical grinding, mechanical polishing and chemical polishing using 50 nm colloidal silica particles. Transmission electron imaging with the scanning electron microscope (TSEM, TESCAN LYRA3, Brno, Czech Republic) [20] is also employed to characterize the microstructures formed in the top surface melted layer and hardened layer. A relatively high acceleration voltage of 30 kV is adopted to enable the electron beam to penetrate the thin-foil specimens, which are prepared via mechanical grinding and twinjet electropolishing. These specimens are firstly mechanically grinded to a thickness of 80  $\mu\text{m}$ , and then electropolished to perforation on a twinjet electropolishing device (Buehler TenuPol5, Lake Bluff, IL, USA) using 10% perchloric acid aqueous solution at a temperature of  $-25\text{ }^\circ\text{C}$  and voltage of 35 V. In addition, phase constitution of the samples is measured using an X-ray diffractometer (XRD, Rigaku Ultima IV, Tokyo, Japan) with  $\text{CuK}\alpha$  radiation, operating at 40 mA and 40 kV with the 2 $\theta$  scan ranging from  $30^\circ$  to  $90^\circ$  at a speed of  $2^\circ/\text{min}$  and step size of  $0.02^\circ$ .

Microhardness measurements are performed on the cross section of samples with applied load of 200 mN using a micro hardness tester (Fischerscope HM2000). Then, the cross-sectional hardness profiles are obtained. Ball-on-disc wear tests are carried out to determine the wear behavior of the samples. GCr15 steel balls (diameter = 5 mm) with hardness of 63–65 HRC serve as the counter body. The ball contacts with the sample surface under a normal load of 100 N and rotates anti-clockwise at a speed of 300 rpm. During the wear process, the weight loss of the samples in a 10 min interval are measured using an electronic microbalance. The wear resistance of the samples is evaluated by the average wear weight loss of its three wear discs. Morphological observations are conducted on the worn surfaces using a TSCAN LYRA3 SEM operating at 20 kV. Meanwhile, the cross-sectional microstructures under the worn surface are examined using EBSD analysis.

Thermal cracking tests are conducted on a homemade thermal fatigue device. The structure of the device and geometry of the specimen can be seen in the literature [21]. In order to accelerate the growth of thermal cracks, the heating temperature of the samples is adopted to  $500\text{ }^\circ\text{C}$ , which is much higher than the service temperature of P20 steel. As a thermal cycling treatment, the surface layers are induction heated from room temperature to  $500\text{ }^\circ\text{C}$  within 7 s at atmospheric environment, and then water cooled to room temperature within 3 s. After 200 to 600 thermal cycles, the specimens are slightly polished for 2 min to remove the oxide layer for the observation of thermal cracks. Additionally, the cross-sectional morphologies of thermal cracks after 600 thermal cycles are also examined using EBSD analysis.

### 3. Results and Discussion

#### 3.1. Characteristics of the Laser-Modified Layer

The microstructures in the surface layer play an important role in the surface performance of the materials. Therefore, microstructure characterizations are mainly focused on the surface layers of the LSE processed samples. The microstructures in the surface melted layer of LSM-2 mm/s sample and in the surface hardened layer of LSH-4 mm/s sample are compared with the initial microstructure of the AR sample, as shown in Figure 3a–c. As seen, the martensite formed in the laser-modified layer is much finer than the initial microstructure. This point is further confirmed by the statistical results of boundary density, which is plotted as the number of boundaries per unit area versus misorientation angle, as shown in Figure 3d–f. The number of boundaries with low misorientation angle ( $2\text{--}15^\circ$ ) and high misorientation angle ( $>50^\circ$ ) are greatly increased in LSM-2 mm/s and LSH-4 mm/s samples, indicating the refinement of microstructure caused by LSE treatment. As well known, the increasing boundary density can greatly improve the strength and hardness, which has a positive effect on the wear and thermal cracking resistance of the materials [22,23]. Therefore, the wear and thermal cracking resistance of the surface layer are expected to be significantly improved by LSE treatment.

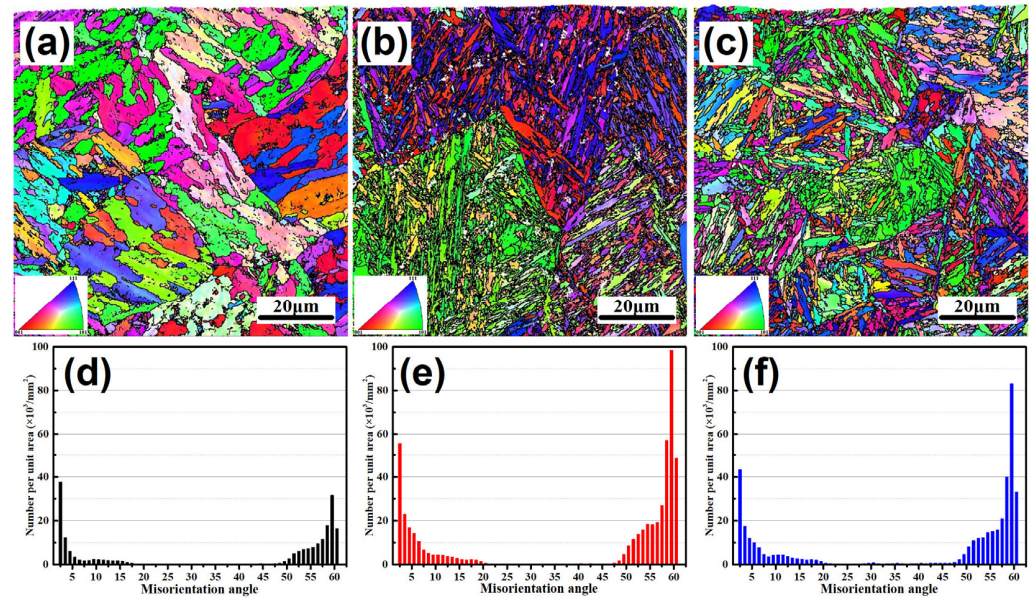


**Figure 3.** Inverse pole figures and corresponding statistical results of boundary density of the cross-sectional microstructures in AR sample (a,d), LSM-2 mm/s sample (b,e) and LSH-4 mm/s sample (c,f).

The microstructures are further observed in detail by TSEM in order to obtain their structural information at high magnification. As shown in Figure 4a,b, lath-type martensite is observed both in the melted layer of LSM-2 mm/s sample and in the hardened layer of LSH-4 mm/s sample. In the XRD patterns embedded in Figure 4, all diffraction peaks correspond to  $\alpha$ -Fe. Residual austenite is not detected by XRD analysis and TESM microstructure observation in these two types of samples. In the melted layer of LSM-2 mm/s sample, a certain amount of acicular carbides are precipitated in the martensite laths, as highlighted in Figure 4a. Nevertheless, the precipitation of carbides are not found in the hardened layer of LSH-4 mm/s sample in Figure 4b. The remarkable auto tempering effect can account for the precipitation of carbides in LSM-2 mm/s sample. Long irradiation time of laser beam on the sample surface caused by low scanning speed increases heat input to the sample surface [24]. The increase of heat input not only leads to the melting of the surface material, but also increases the time required for the modified layer to cool to room temperature. Hence, the autotempering effect is more pronounced at low scanning speed [25], giving rise to the precipitation of carbides in the melted layer of LSM-2 mm/s sample.

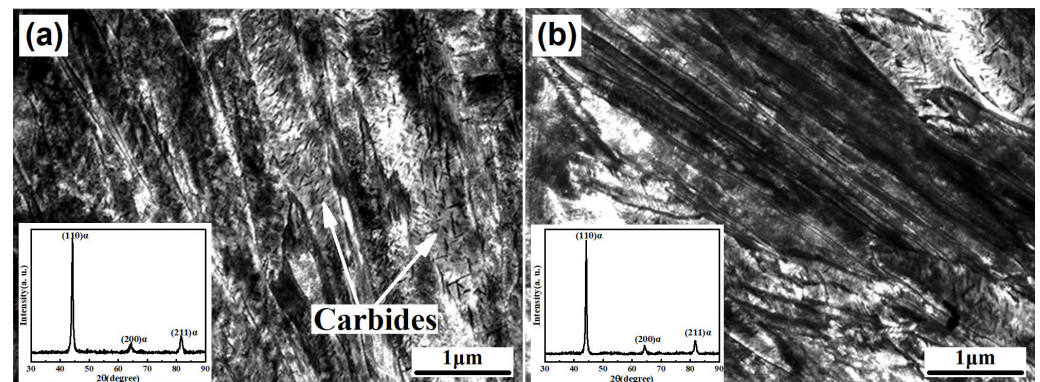


**Figure 4.** TSEM pictures and XRD patterns of the microstructures formed in the melted layer of LSM-2 mm/s sample (a) and hardened layer of LSH-4 mm/s sample (b).

Figure 5 shows the cross-sectional hardness profiles of AR and LSE processed samples. Case depths of 1530  $\mu\text{m}$  and 1034  $\mu\text{m}$  are detected for LSM-2 mm/s sample and LSH-4 mm/s sample, respectively. These values are consistent with the results obtained by

cross sectional macrostructure observation in Figure 2. For LSM-2 mm/s and LSH-4 mm/s samples, the average hardness of the laser-modified layer is found to be 607 HV and 655 HV, respectively, which is 73% and 87% higher than that of the P20 substrate. The great improvement in hardness is mainly attributed to the solid-solution strengthening effect caused by carbon and alloy elements and the Hall–Petch strengthening effect of microstructure refinement, which originate from the generation of martensite in these modified layer. Although the LSM-2 mm/s sample exhibits a deeper modified layer, the average hardness of its modified layer is lower than that of the LSH-4 mm/s sample. It seems that low scanning speed results in a decreased surface hardness in the present work. As previously mentioned, low scanning speed increases heat input to the sample surface and induces a pronounced autotempering effect. This can be regarded as the main reason for the relatively low hardness of the modified layer in LSM-2 mm/s sample. Besides, the contents of alloy elements (Si, Mn, Cr, V and Al) in the surface melted layer of LSM-2 mm/s sample are obviously lower in comparison with the surface layer of LSH-4 mm/s sample and the AR material, as shown in Table 1. It can be inferred that vaporization of these alloy elements occurs during the melting of surface material. The reduction of alloy element content in the surface melted layer of LSM-2 mm/s sample is another reason for its relatively low hardness compared with LSH-4 mm/s sample.

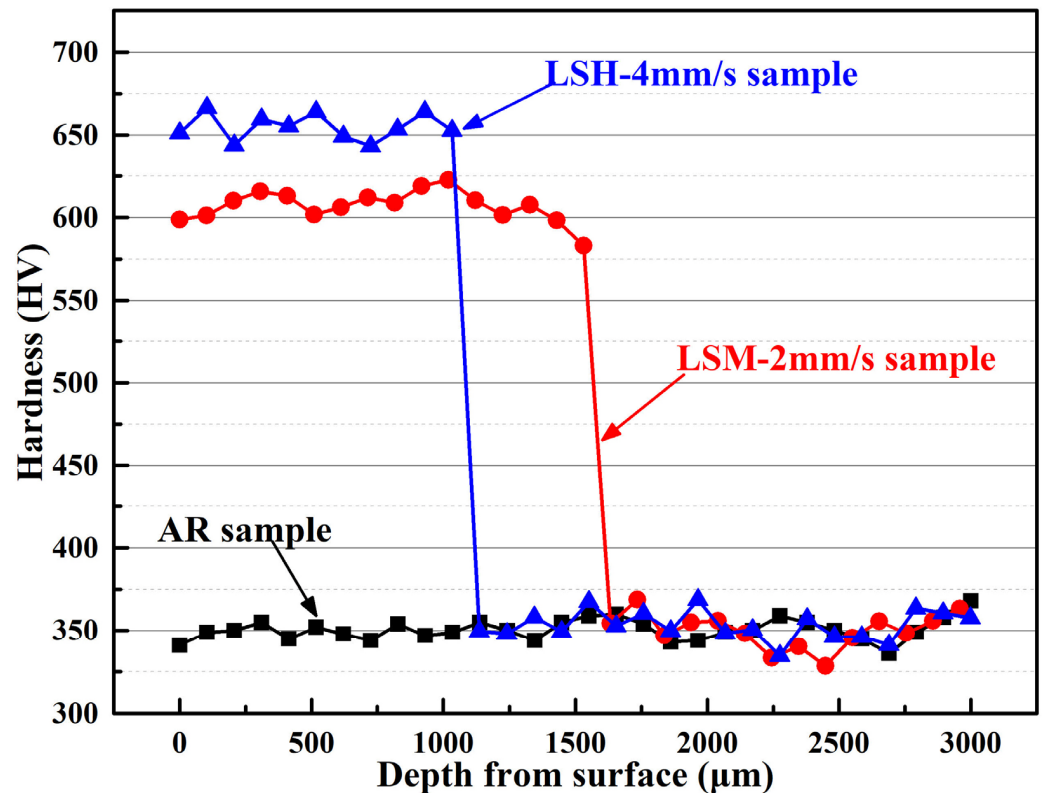
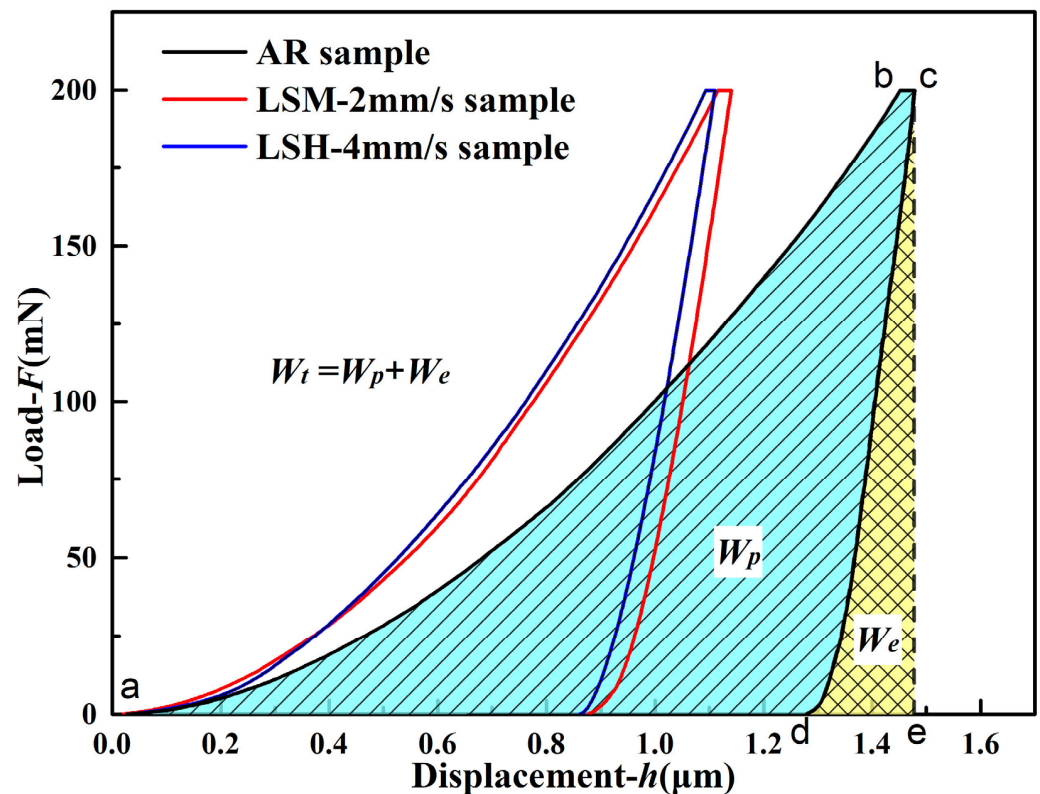


Figure 5. Hardness profiles versus depth of the AR sample and LSE processed samples.

The mechanical behavior of the P20 substrate and laser-modified layers are estimated by the load-displacement (F-h) curves, which are recorded during indentation hardness tests. F is the load applied during the test, while h is the depth of the indenter penetrated into the sample surface. As marked on the curve of P20 substrate in Figure 6, the load-displacement curve includes three segments: loading (a-b), holding (b-c) and unloading (c-d). The relationship between load F and indenter displacement h during the loading segment can be described as  $F = C \times h^2$ , where C is the loading curvature. According to the literature [26], a high value of C represents the excellent resistance of the material to indentation. The values of C determined by data fitting are 97.26, 163.44 and 169.71 mN/ $\mu\text{m}^2$  respectively for P20 substrate, surface melted layer of LSM-2 mm/s sample and surface

hardened layer of LSH-4 mm/s sample. It can be deduced that the indentation resistance increases in the order of AR sample, LSM-2 mm/s sample and LSH-4 mm/s sample. In addition, some researchers [27] have proposed that the plastic deformation resistance of materials can be evaluated by plasticity factor  $\eta_p$ , which is equal to the ratio of plastic deformation work  $W_p$  to the total deformation work  $W_t$ .  $W_t$  is the sum of plastic deformation work  $W_p$  and elastic deformation work  $W_e$ , as shown in Figure 6. A small plasticity factor  $\eta_p$  indicates great resistance to plastic deformation. The value of  $\eta_p$  for the P20 substrate, top surface layers of LSM-2 mm/s sample and LSH-4 mm/s sample is 0.85, 0.76 and 0.74, respectively. It is evident that LSM-2 mm/s and LSH-4 mm/s samples exhibit superior plastic deformation resistance compared with AR sample.



**Figure 6.** Representative load-displacement curves for P20 substrate and laser-modified layers with different scanning speed.

### 3.2. Evaluation of Wear Resistance

The weight loss curves of AR, LSM-2 mm/s and LSH-4 mm/s samples are shown in Figure 7. The weight loss after a sliding distance of 1400 m is 38.4 mg for AR sample, whereas this value decreases to 18.8 mg and 9.4 mg for the LSM-2 mm/s sample and LSH-4 mm/s sample, respectively. High weight loss of AR sample manifests the poor wear resistance due to its low surface hardness. Compared with the AR sample, LSH-4 mm/s sample exhibits about 75.5% reduction in weight loss, indicating a significant improvement in wear resistance. LSM treatment with scanning speed of 2 mm/s also improves the wear resistance to some extent. However, the weight loss of LSM-2 mm/s sample is slightly higher than that of the LSH-4 mm/s sample. It can be inferred that the wear resistance of the samples increases in the order of AR sample, LSM-2 mm/s sample, LSH-4 mm/s sample. This is in accordance with the surface hardness of these samples. High surface hardness is recognized as a favorable factor for the material to resist the wear and tear [28,29]. The formation of martensite with high hardness in the surface layer endows P20 steel with excellent wear resistance.

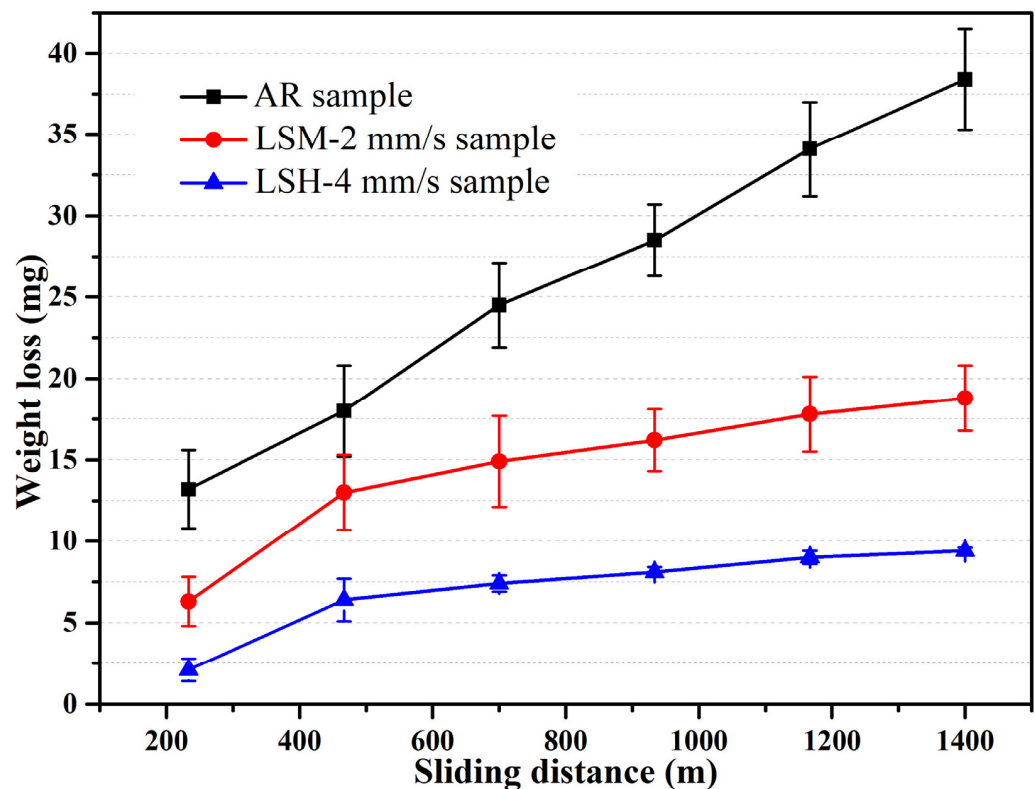
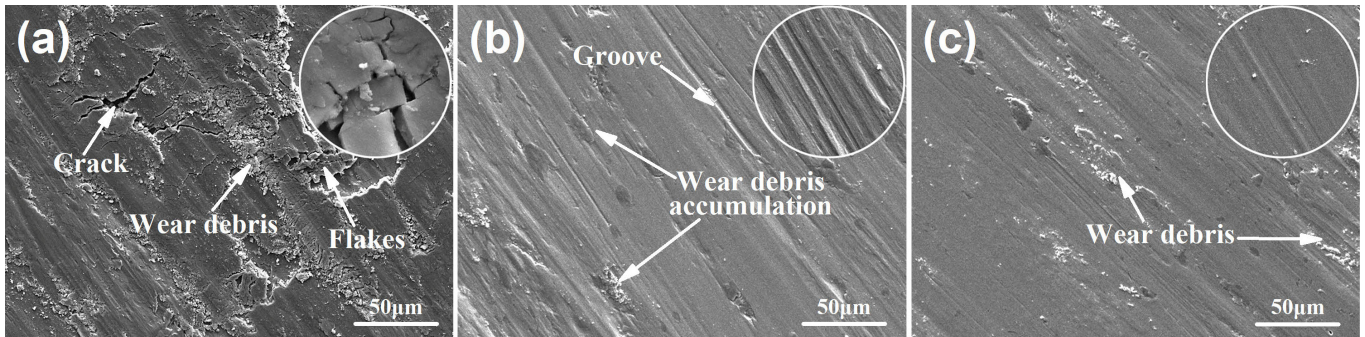


Figure 7. Weight loss as a function of sliding distance of samples in different states.

As noted in connection with Figure 7, the weight loss of these samples exhibits different trends with the increasing sliding distance. The weight loss of AR sample increases linearly with sliding distance. By contrast, the weight loss curves of LSM-2 mm/s and LSH-4 mm/s samples can be segmented into two stages. The initial stage (sliding distance  $\leq 470$  m) with a high wear rate is in the fretting wear stage [30]. Then, steady-state wear stage with decreased wear rate is reached when the sliding distance exceeds 470 m. The wear behavior is closely related to the wear mechanism. Therefore, the worn surfaces are observed in detail by scanning electron microscope in order to determine the wear mechanism that occurred in these samples. The representative worn morphologies are demonstrated in Figure 8. For AR specimens, plenty of debris are found with cracks and flakes on its worn surface, as exhibited in Figure 8a. The development of surface cracks is generally concerned with the accumulation of plastic deformation in surface material [31]. Hence, it can be inferred that the surface material experiences severe plastic deformation under the cyclic load. These cracks gradually grow up during repeated plastic deformation, thus leading to the detachment of surface material and resulting in a serious material loss. Large pits are developed on the worn surface resulting from the successive shedding of flakes. In the following sliding process, the crushed flakes acting as wear particles give rise to abrasive wear. Based on the above analysis, it can be deduced that successive shedding of flakes induced by surface cracks propagation accompanying with abrasive wear are the main wear mechanism for AR specimen.

LSM-2 mm/s sample and LSH-4 mm/s sample exhibit a smooth worn surface. Cracks and large flakes caused by surface plastic deformation are not observed on their worn surfaces. The wear debris and grooves in Figure 8b,c demonstrate that abrasive wear and adhesive wear are the main wear mechanism for the LSE processed samples. These characteristics of the worn surface indicate reduced wear damage and improved wear resistance both in LSM-2 mm/s sample and in LSH-4 mm/s sample. However, the weight loss curves in Figure 7 demonstrate that LSH-4 mm/s sample possesses higher wear resistance than the LSM-2 mm/s sample. This point is confirmed by the relatively shallow abrasion grooves on the worn surface of LSH-4 mm/s sample, as shown in Figure 8c.

It is well known that surface hardness plays an important role in determining the wear resistance of materials. Therefore, the superior wear resistance of LSH-4 mm/s sample is attributed to its highest surface hardness.



**Figure 8.** Worn surfaces for the AR sample (a), LSM-2 mm/s sample (b) and LSH-4 mm/s sample (c).

To observe the evolution of surface microstructure in the process of wear experiment, a cross sectional observation is performed on the mid region of wear trace using EBSD measurement. As shown in Figure 9a, a wear induced refinement layer with a thickness of about 50 μm is formed on the surface of AR sample. By contrast, relatively thin refinement layers are presented in Figure 9b,c for the LSE samples. The formation of the refinement layer is generally related to the plastic deformation induced by the cyclic loading [32–34]. According to the results implied in Figure 6, the laser-modified layers with high hardness martensite have excellent plastic deformation resistance, whereas the P20 substrate exhibits an inferior deformation resistance. Therefore, a deeper refinement layer is found on the cross section of AR sample. The severe plastic deformation of surface material results in the formation of cracks and the shedding of flakes [35]. Then, a new plastic deformation layer will gradually generate in the subsequent wear process and fall off from the worn surface again. Consequently, a linear increase of weight loss with sliding distance is recorded for the AR sample. By contrast, the martensite with high hardness in the laser-modified layer effectively prevents the occurrence of plastic deformation. Therefore, a steady-state wear stage with decreased wear rate is reached after a sliding distance of 470 m.

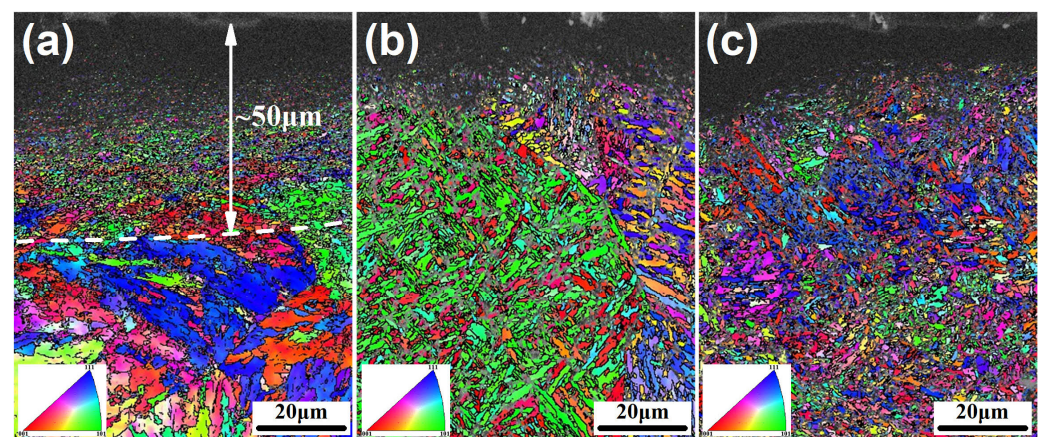


**Figure 9.** Inverse pole figures showing the microstructure evolution under the wear scar in the AR sample (a), LSM-2 mm/s sample (b) and LSH-4 mm/s sample (c).

### 3.3. Evaluation of Thermal Cracking Behavior

The propagation behaviors of thermal cracks in AR and LSE processed samples after different thermal cycles are illustrated in Figure 10. The surface thermal cracks in all samples grow up gradually both in length and width with the increase of thermal cycles. For AR sample, plenty of thermal cracks are formed on the surface after 200 thermal cycles.

These thermal cracks propagate along irregular paths and generate branch cracks after 400 thermal cycles. With the formation of new cracks, the old cracks connect into a crack network after 600 thermal cycles, as shown in Figure 10a1–a3. The severe thermal crack network on the surface of AR sample indicates its poor resistance to thermal cracking. In contrast, the thermal cracks in LSE samples exhibit significant difference in propagation behavior. For the LSM-2 mm/s sample and LSH-4 mm/s sample, the thermal cracks formed after 200 thermal cycles are obviously less than that of the AR sample, as shown in Figure 10b1,c1. Moreover, the thermal cracks propagate in a relatively straight path after 400 thermal cycles in Figure 10b2,c2. The absence of crack intertwining in Figure 10b3,c3 indicates excellent thermal cracking resistance even after 600 thermal cycles. It is obvious that the number of thermal cracks of LSE-4 mm/s sample is minimum, indicating the greatest resistance to thermal cracking.

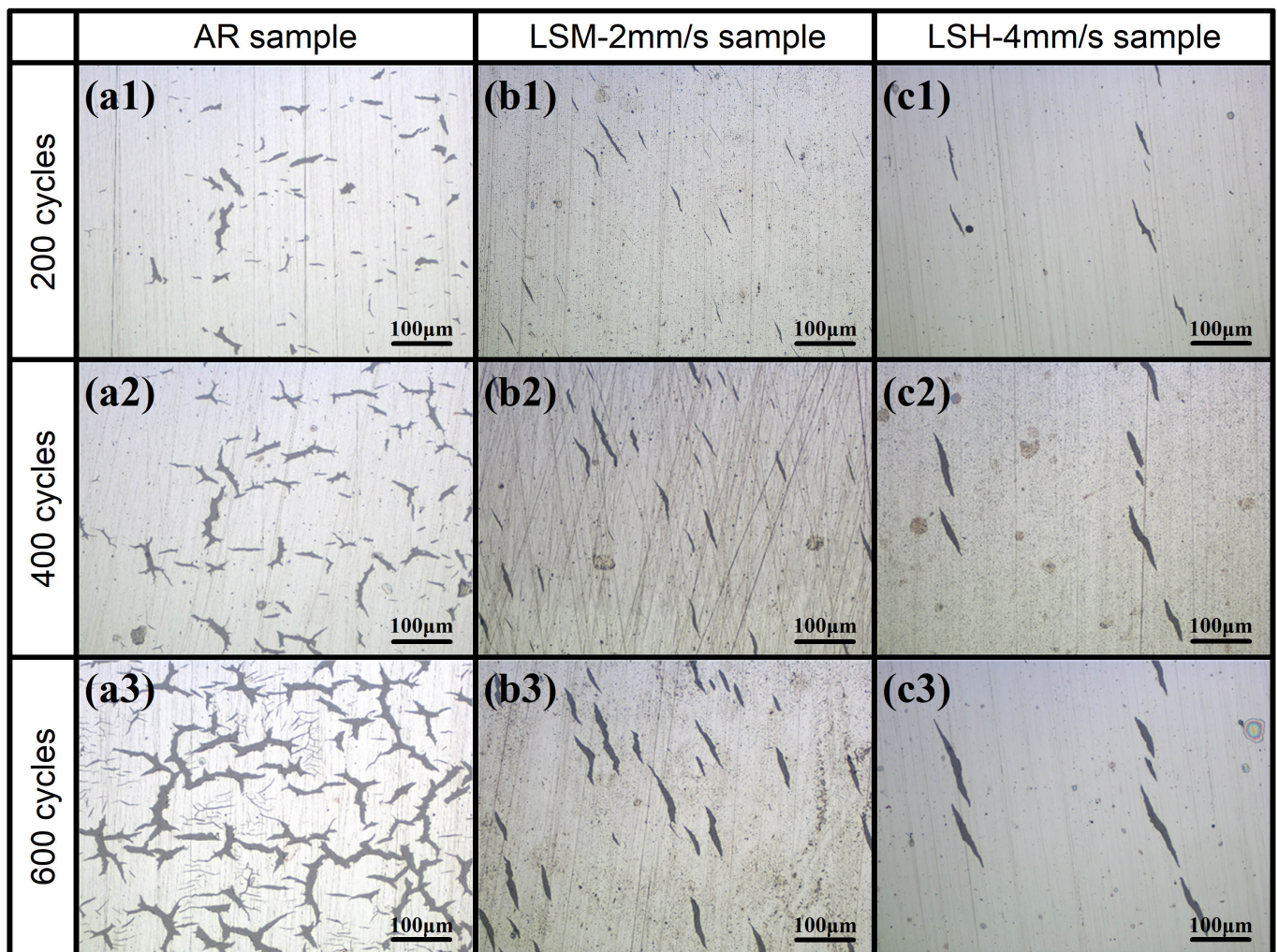


**Figure 10.** Morphologies of thermal cracks formed on the surface of AR sample (a1–a3), LSM-2 mm/s sample (b1–b3) and LSH-4 mm/s sample (c1–c3) after different thermal cycles.

In order to elucidate the propagation of thermal cracks more clearly, the morphologies of the thermal cracks in cross section of the samples are observed by EBSD measurement, and the results are shown in Figure 11. The crack length in the cross section of AR sample is obviously larger than that of the LSE samples. Moreover, a strain-induced refinement layer with a thickness of about 13  $\mu\text{m}$  is observed on the surface of AR sample, as shown in Figure 11a. Similar to the formation of cracks on the worn surface, the nucleation of thermal crack is also closely related to the plastic deformation accumulated in the surface material. The accumulation of plastic strain in the surface material promotes the nucleation of thermal

crack [36,37]. The martensite with high plastic deformation resistance in the laser-modified layer effectively reduces the plastic strain of the surface material. Therefore, relatively thin strain-induced refinement layers are observed on the cross sections of LSM-2 mm/s and LSH-4 mm/s samples, as shown in Figure 11b,c. This is the reason that fewer thermal cracks are formed on the surface of LSM-2 mm/s and LSH-4 mm/s samples compared with AR sample.

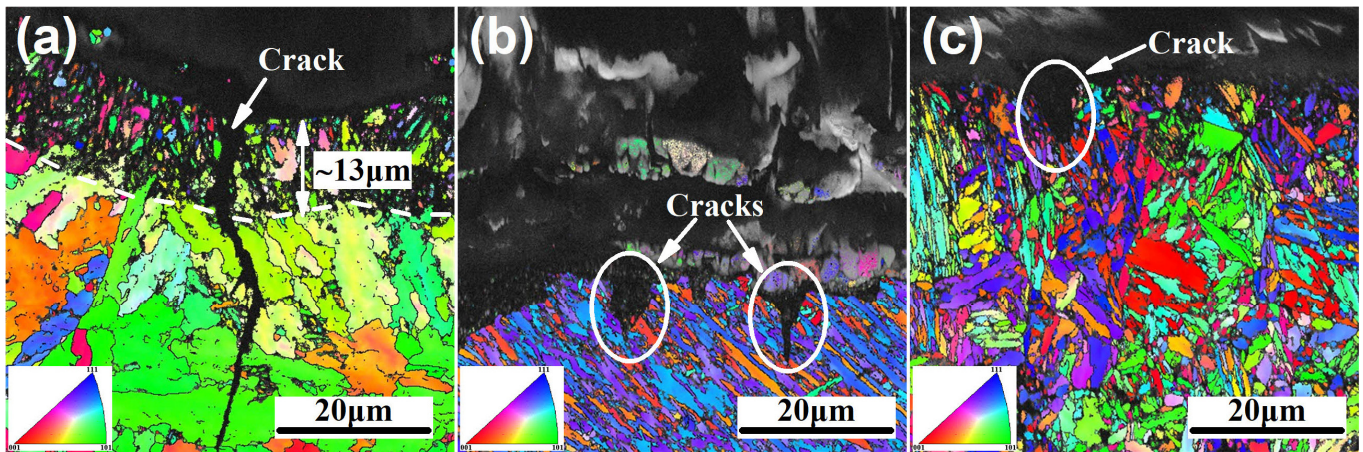


**Figure 11.** Typical morphologies of the thermal cracks in cross section of the AR sample (a), LSM-2 mm/s sample (b) and LSH-4 mm/s sample (c) after 600 cycles.

In addition, it also can be seen that the thermal cracks in Figure 11 propagate through the sub-units of the microstructure in all three types of samples, indicating a transgranular type of cracking. The boundaries in the microstructure are the main obstacles to the crack propagation for the transgranular type of cracking [38]. More energy will be consumed when the thermal crack passes through these boundaries. Therefore, it can be deduced that the increase of boundary density or refinement of microstructure in the laser-modified layer hinder the thermal crack propagation. Moreover, initial high hardness of the laser-modified layers can induce a low softening rate during the test [39]. It is also beneficial to hinder the propagation of thermal cracks. As a conclusion, LSE treatment effectively suppresses the nucleation and propagation of thermal cracks by producing fine martensite with high plastic deformation resistance in the surface layer.

#### 4. Conclusions

In this work, LSE is applied to P20 plastic mold steel in order to modify wear resistance and thermal cracking resistance by controlling the surface microstructure and hardness. The major conclusions are summarized as follows:

- (1) LSE treatment with low scanning speed ( $\leq 2$  mm/s) and high scanning speed ( $\geq 3$  mm/s) leads to the surface melting and surface hardening, respectively. LSH treatment with scanning speed of 4 mm/s exhibits a greater improvement in surface hardness and plastic deformation resistance than LSM treatment with scanning speed of 2 mm/s. Lath-type martensite is formed in all the laser-modified layers. However, the precipitation of carbides inside the martensite lath caused by the pronounced autotempering effect and the vaporization of alloy elements in the melted layer of LSM-2 mm/s sample gives rise to the relatively low surface hardness and plastic deformation resistance compared with LSH-4 mm/s sample.
- (2) The wear mechanism changes from successive shedding of flakes for P20 substrate to combination of abrasive and adhesive wear for laser-modified layer. LSE treatment inhibits surface plastic deformation during wear tests, thus suppressing the generation of surface cracks and the shedding of flakes. A significant improvement of wear resistance is recorded for the LSE processed sample. However, LSH-4 mm/s

sample exhibits greater wear resistance due to its higher surface hardness and plastic deformation resistance in comparison with LSM-2 mm/s sample.

- (3) The thermal crack network formed on AR sample indicates a poor thermal cracking resistance of the AR P20 steel. The thermal cracking resistance of this material is drastically improved by LSE treatment. For the laser-modified layers, high surface hardness and plastic deformation resistance suppress the nucleation of thermal cracks, while the high boundary density hinders the propagation of these cracks.

**Author Contributions:** Validation, C.L.; investigation, J.L. and W.G.; writing—original draft preparation, K.Z.; writing—review and editing, G.Y.; supervision, J.G.; funding acquisition, C.L. All authors have read and agreed to the published version of the manuscript.

**Funding:** This research was funded by the National Natural Science Foundation of China (52171042), Natural Science Foundation of Shandong Province (ZR2020MA049) and the Innovation Ability Improvement Project for small and medium-sized high-tech company in Shandong Province (2021TSGC1017).

**Institutional Review Board Statement:** Not applicable.

**Informed Consent Statement:** Not applicable.

**Data Availability Statement:** Not applicable.

**Conflicts of Interest:** The authors declare no conflict of interest.

## References

1. Li, H.; Qi, H.; Song, C.; Li, Y.; Yan, M. Selective laser melting of P20 mould steel: Investigation on the resultant microstructure, high-temperature hardness and corrosion resistance. *Powder Metall.* **2018**, *61*, 21–27. [[CrossRef](#)]
2. Park, C.; Sim, A.; Ahn, S.; Kang, H.; Chun, E.J. Influence of laser surface engineering of AISI P20-improved mold steel on wear and corrosion behaviors. *Surf. Coat. Technol.* **2019**, *377*, 124852. [[CrossRef](#)]
3. Harlin, P.; Bexell, U.; Olsson, M. Influence of surface topography of arc-deposited TiN and sputter-deposited WC/C coatings on the initial material transfer tendency and friction characteristics under dry sliding contact conditions. *Surf. Coat. Technol.* **2009**, *203*, 1748–1755. [[CrossRef](#)]
4. Soriano, C.; Leunda, J.; Lambarri, J.; García Navas, V.; Sanz, C. Effect of laser surface hardening on the microstructure, hardness and residual stresses of austempered ductile iron grades. *Appl. Surf. Sci.* **2011**, *257*, 7101–7106. [[CrossRef](#)]
5. Senthil Selvan, J.; Subramanian, K.; Nath, A. Effect of laser surface hardening on En18 (AISI 5135) steel. *J. Mater. Process. Technol.* **1999**, *91*, 29–36. [[CrossRef](#)]
6. Jia, Z.; Liu, Y.; Li, J.; Liu, L.; Li, H. Crack growth behavior at thermal fatigue of H13 tool steel processed by laser surface melting. *Int. J. Fatigue* **2015**, *78*, 61–71. [[CrossRef](#)]
7. Cordovilla, F.; García-Beltrán, Á.; Domínguez, J.; Sancho, P.; Ocaña, J.L. Numerical-experimental analysis of the effect of surface oxidation on the laser transformation hardening of Cr–Mo steels. *Appl. Surf. Sci.* **2015**, *357*, 1236–1243. [[CrossRef](#)]
8. Chiang, K.A.; Chen, Y.C. Laser surface hardening of H13 steel in the melt case. *Mater. Lett.* **2005**, *59*, 1919–1923. [[CrossRef](#)]
9. Chen, Z.; Zhu, Q.; Wang, J.; Yun, X.; He, B.; Luo, J. Behaviors of 40Cr steel treated by laser quenching on impact abrasive wear. *Opt. Laser. Technol.* **2018**, *103*, 118–125. [[CrossRef](#)]
10. Telasang, G.; Majumdar, J.D.; Padmanabham, G.; Manna, I. Wear and corrosion behavior of laser surface engineered AISI H13 hot working tool steel. *Surf. Coat. Technol.* **2015**, *261*, 69–78. [[CrossRef](#)]
11. Pantelis, D.; Bouyiouri, E.; Kouloumbi, N.; Vassiliou, P.; Koutsomichalis, A. Wear and corrosion resistance of laser surface hardened structural steel. *Surf. Coat. Technol.* **2002**, *161*, 125–134. [[CrossRef](#)]
12. Mahmoudi, B.; Torkamany, M.; Aghdam, A.S.R.; Sabbaghzade, J. Laser surface hardening of AISI 420 stainless steel treated by pulsed Nd:YAG laser. *Mater. Des.* **2010**, *31*, 2553–2560. [[CrossRef](#)]
13. Kwok, C.; Cheng, F.; Man, H. Microstructure and corrosion behavior of laser surface-melted high-speed steels. *Surf. Coat. Technol.* **2007**, *202*, 336–348. [[CrossRef](#)]
14. Moradi, M.; Ghorbani, D.; Moghadam, M.K.; Kazazi, M.; Rouzbahani, F.; Karazi, S. Nd: YAG laser hardening of AISI 410 stainless steel: Microstructural evaluation, mechanical properties, and corrosion behavior. *J. Alloys Compd.* **2019**, *795*, 213–222. [[CrossRef](#)]
15. Preece, C.; Draper, C. The effect of laser quenching the surfaces of steels on their cavitation erosion resistance. *Wear* **1981**, *67*, 321–328. [[CrossRef](#)]
16. Zhang, Z.; Lin, P.; Zhou, H.; Ren, L. Microstructure, hardness, and thermal fatigue behavior of H21 steel processed by laser surface remelting. *Appl. Surf. Sci.* **2013**, *276*, 62–67. [[CrossRef](#)]
17. Colaço, R.; Vilar, R. Stabilisation of retained austenite in laser surface melted tool steels. *Mater. Sci. Eng. A* **2004**, *385*, 123–127. [[CrossRef](#)]

18. Ameri, M.; Ghaini, F.M.; Torkamany, M. Investigation into the efficiency of a fiber laser in surface hardening of ICD-5 tool steel. *Opt. Laser. Technol.* **2018**, *107*, 150–157. [[CrossRef](#)]
19. Van Brussel, B.; Hegge, H.; De Hosson, J.T.M.; Delhez, R.; De Keijser, T.H.; Van der Pers, N. Development of residual stress and surface cracks in laser treated low carbon steel. *Scr. Metal. Mater.* **1991**, *25*, 779–784. [[CrossRef](#)]
20. Klein, T.; Buhr, E.; Frase, C.G. TSEM: A review of scanning electron microscopy in transmission mode and its applications. In *Advances in Imaging and Electron Physics*; Peter, W.H., Martin, H., Eds.; Elsevier: Braunschweig, Germany, 2012; pp. 297–356.
21. Liu, B.; Wang, B.; Yang, X.; Zhao, X.; Qin, M.; Gu, J. Thermal fatigue evaluation of AISI H13 steels surface modified by gas nitriding with pre-and post-shot peening. *Appl. Surf. Sci.* **2019**, *483*, 45–51. [[CrossRef](#)]
22. Zhu, K.; Bouaziz, O.; Oberbillig, C.; Huang, M. An approach to define the effective lath size controlling yield strength of bainite. *Mater. Sci. Eng. A* **2010**, *527*, 6614–6619. [[CrossRef](#)]
23. Jiang, J.; Wu, H.; Liang, J.; Tang, D. Microstructural characterization and impact toughness of a jackup rig rack steel treated by intercritical heat treatment. *Mater. Sci. Eng. A* **2013**, *587*, 359–364. [[CrossRef](#)]
24. Santhanakrishnan, S.; Kovacevic, R. Hardness prediction in multi-pass direct diode laser heat treatment by on-line surface temperature monitoring. *J. Mater. Process. Technol.* **2012**, *212*, 2261–2271. [[CrossRef](#)]
25. Shiue, R.; Chen, C. Laser transformation hardening of tempered 4340 steel. *Metall. Trans. A* **1992**, *23*, 163–170. [[CrossRef](#)]
26. Giannakopoulos, A.; Suresh, S. Determination of elastoplastic properties by instrumented sharp indentation. *Scr. Mater.* **1999**, *40*, 1191–1198. [[CrossRef](#)]
27. Yan, M.; Wu, Y.; Liu, R. Plasticity and ab initio characterizations on Fe<sub>4</sub>N produced on the surface of nanocrystallized 18Ni-maraging steel plasma nitrided at lower temperature. *Appl. Surf. Sci.* **2009**, *255*, 8902–8906. [[CrossRef](#)]
28. Zhao, X.; Wang, B.; Sun, D.; Li, C.; Han, L.; Gu, J. Effect of pre-existing VC carbides on nitriding and wear behavior of hot-work die steel. *Appl. Surf. Sci.* **2019**, *486*, 179–186. [[CrossRef](#)]
29. Yan, M.; Wang, Y.; Chen, X.; Guo, L.; Zhang, C.; You, Y.; Bai, B.; Chen, L.; Long, Z.; Li, R. Laser quenching of plasma nitrided 30CrMnSiA steel. *Mater. Des.* **2014**, *58*, 154–160. [[CrossRef](#)]
30. Amanov, A.; Umarov, R. The effects of ultrasonic nanocrystal surface modification temperature on the mechanical properties and fretting wear resistance of Inconel 690 alloy. *Appl. Surf. Sci.* **2018**, *441*, 515–529. [[CrossRef](#)]
31. Pan, R.; Ren, R.; Zhao, X.; Chen, C. Influence of microstructure evolution during the sliding wear of CL65 steel. *Wear* **2018**, *400*, 169–176. [[CrossRef](#)]
32. Gola, A.; Ghadamgahi, M.; Ooi, S. Microstructure evolution of carbide-free bainitic steels under abrasive wear conditions. *Wear* **2017**, *376*, 975–982. [[CrossRef](#)]
33. Sun, H.; Shi, Y.; Zhang, M.X. Sliding wear-induced microstructure evolution of nanocrystalline and coarse-grained AZ91D Mg alloy. *Wear* **2009**, *266*, 666–670. [[CrossRef](#)]
34. Rigney, D.A.; Karthikeyan, S. The evolution of tribomaterial during sliding: A brief introduction. *Tribol. Lett.* **2010**, *39*, 3–7. [[CrossRef](#)]
35. Rice, S.L.; Nowotny, H.; Wayne, S.F. Characteristics of metallic subsurface zones in sliding and impact wear. *Wear* **1981**, *74*, 131–142. [[CrossRef](#)]
36. Klobčar, D.; Kosec, L.; Kosec, B.; Tušek, J. Thermo fatigue cracking of die casting dies. *Eng. Fail. Anal.* **2012**, *20*, 43–53. [[CrossRef](#)]
37. Klobčar, D.; Tušek, J.; Taljat, B. Thermal fatigue of materials for die-casting tooling. *Mater. Sci. Eng. A* **2008**, *472*, 198–207. [[CrossRef](#)]
38. Zhao, X.; Zhang, H.; Liu, Y. Effect of laser surface remelting on the fatigue crack propagation rate of 40Cr steel. *Results Phys.* **2019**, *12*, 424–431. [[CrossRef](#)]
39. Persson, A.; Hogmark, S.; Bergström, J. Simulation and evaluation of thermal fatigue cracking of hot work tool steels. *Int. J. Fatigue* **2004**, *26*, 1095–1107. [[CrossRef](#)]

**Disclaimer/Publisher’s Note:** The statements, opinions and data contained in all publications are solely those of the individual author(s) and contributor(s) and not of MDPI and/or the editor(s). MDPI and/or the editor(s) disclaim responsibility for any injury to people or property resulting from any ideas, methods, instructions or products referred to in the content.